Case Studies in Thermal Engineering 81 (2026) 108012

Contents lists available at ScienceDirect

Case Studies in Thermal Engineering

journal homepage: www.elsevier.com/locate/csite

Failure analysis and degradation mechanisms of GX130CrSi29 grate bars in a biomass-fired furnace: An industrial case study

Wirasak Khongkaew [a], Natt Makul [b], Kewalee Nilgumhang [c], Phadungsak Rattanadecho [a,*]

[a] Hub of Talents Electromagnetic Energy Utilization in Engineering, Department of Mechanical Engineering, Faculty of Engineering, Thammasat University, Rangsit Campus, Pathum Thani, 12120, Thailand
[b] Department of Civil Engineering Technology, Faculty of Industrial Technology, Phranakhon Rajabhat University, Changwattana Road, Bangkhen, Bangkok, 10220, Thailand
[c] Nuclear Engineering and Technology Center (NETC), Thailand Institute of Nuclear Technology (Public Organization), Ongkarak District, Nakhon Nayok Province, 26120, Thailand

GRAPHICAL ABSTRACT

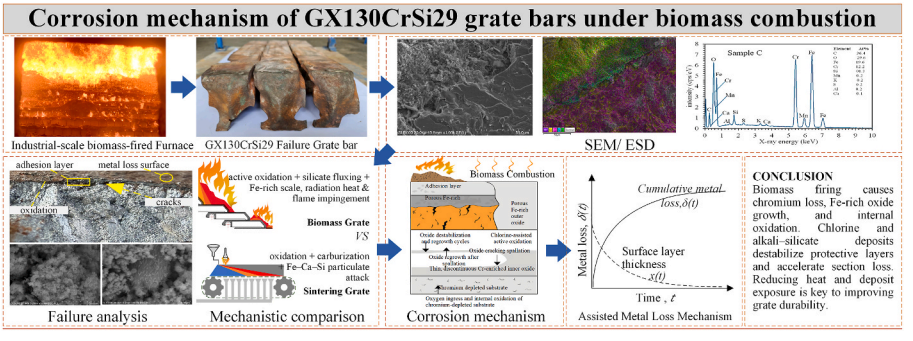

ARTICLE INFO

Keywords:
Biomass-fired furnace
Grate bar failure
Alkali–chloride corrosion
Active oxidation
Thermochemical degradation
Flow-assisted removal

ABSTRACT

Premature degradation of grate bars is a persistent operational challenge in biomass-fired furnaces, particularly when alkali-rich fuels are used, leading to increased maintenance and unplanned outages. Although biomass combustion and ash chemistry have been widely investigated, detailed failure analyses based on service-exposed grate components from operating power plants remain relatively limited. This study investigates the degradation behavior of GX130CrSi29 grate bars retrieved from a 9.9 MW rubberwood-fired reciprocating grate furnace. Failed components

* Corresponding author.
E-mail address: ratphadu@engr.tu.ac.th (P. Rattanadecho).

https://doi.org/10.1016/j.csite.2026.108012
Received 8 January 2026; Received in revised form 22 March 2026; Accepted 31 March 2026
Available online 1 April 2026

Industrial case study
SEM/EDS analysis

collected during scheduled maintenance were examined using a practical failure-analysis approach combining macroscopic inspection with cross-sectional field-emission scanning electron microscopy and energy-dispersive X-ray spectroscopy (FE-SEM/EDS), including elemental mapping and line-scan analysis. The results reveal a reproducible multilayer degradation architecture consisting of (i) an outer adhesion layer enriched in K-, Ca-, and Si-bearing ash deposits, (ii) a porous iron-rich oxide scale, and (iii) a chromium-depleted substrate exhibiting internal oxidation. Elemental distributions show pronounced chromium depletion near the oxide–metal interface together with chlorine- and alkali-bearing deposits. These microstructural and chemical features are consistent with degradation involving chlorine-assisted active oxidation and alkali–silicate-related fluxing under biomass combustion conditions. The position-dependent and non-uniform section loss observed in the grate bars is interpreted using a coupled thermochemical corrosion and flow-assisted removal framework, in which corrosion-weakened oxide and deposit layers may be intermittently detached under localized gas-flow interaction and high thermal loading. Although conceptual rather than predictive, this framework provides a physically consistent interpretation of the irregular degradation patterns observed in service. The findings highlight the dominant role of biomass ash chemistry and furnace operating conditions in controlling grate degradation and provide practical insights for grate material selection and operational strategies in biomass-fired power systems.

1. Introduction

Biomass-fired power plants increasingly employ moving- and reciprocating-grate combustion systems owing to their fuel flexibility, operational simplicity, and suitability for decentralized energy production. Such systems are widely applied for the utilization of agricultural residues and woody biomass. However, premature failure of grate bars remains a persistent operational challenge, frequently leading to unplanned shutdowns, reduced thermal efficiency, and increased maintenance costs. Practical operating experience indicates that grate degradation in biomass-fired furnaces is strongly governed by the aggressive thermochemical environment inherent to biomass combustion, which is characterized by elevated concentrations of alkali metals, chlorine, sulfur, and siliceous ash components [1,2,3].

In grate-fired biomass furnaces, potassium-rich species released from the fuel readily condense or deposit on hot grate surfaces. In the presence of chlorine and silica, these deposits participate in complex thermochemical interactions that differ fundamentally from those encountered in coal-fired or mineral-based combustion systems. Previous studies on grate-fired boilers have primarily focused on combustion behavior, temperature distribution, gas composition, and flow characteristics within the fuel bed [4,2,3,5–12]. While these studies provide valuable insight into furnace performance and operating conditions, they offer limited information regarding the degradation pathways governing grate-bar failure under real full-scale operating conditions.

High-temperature degradation of heat-resistant cast steels has been extensively investigated in environments such as gas turbines, coal-fired boilers, waste incinerators, and iron ore sintering furnaces [13,14–16]. In these systems, degradation is typically dominated by oxidation, carburization, or sulfidation mechanisms. Biomass combustion, however, introduces additional complexity due to the simultaneous presence of potassium, chlorine, and silicon, which promotes aggressive alkali–chloride–silicate interactions and significantly accelerates material degradation compared with classical oxidation-controlled environments [17–19].

Chlorine plays a central role in biomass-related corrosion and exists both in the gas phase, primarily as HCl, and in condensed deposits as alkali chlorides such as KCl. At elevated temperatures, chlorine participates in active oxidation cycles by reacting with metallic elements at the oxide–metal interface to form volatile metal chlorides. Subsequent oxidation of these chlorides generates non-protective oxides while regenerating chlorine, thereby sustaining degradation [17,18]. For chromium-containing alloys, interactions between alkali chlorides and chromium-rich surface layers destabilize protective oxides and promote chromium depletion, accelerating metal loss [14,20].

In parallel, potassium released during biomass combustion readily reacts with siliceous ash components to form low-melting potassium–silicate compounds. At typical grate operating temperatures, these compounds may exist in molten or semi-molten states and act as effective fluxing agents, dissolving or penetrating protective oxide layers and exposing the underlying metal to intensified chemical attack [21]. As a result, severe grate degradation is generally attributed to the synergistic interaction between chlorine-induced active oxidation and molten-phase fluxing rather than to simple high-temperature oxidation alone [18,19].

Although chlorine- and alkali-induced corrosion mechanisms have been widely discussed, most existing studies rely on laboratory-scale exposures, simplified deposit chemistries, or surrogate materials. Systematic investigations based on microstructural evidence from failed grate bars retrieved from full-scale biomass power plants remain limited. Fan et al. [13] reported layered corrosion scales, carburization, and chromium-depleted zones in grate bars from iron ore sintering furnaces; however, the chemical environment in such furnaces lacks the intense alkali–chloride–silicate chemistry characteristic of biomass combustion. Consequently, degradation mechanisms identified for sintering applications cannot be directly extrapolated to biomass-fired grate systems.

To address this gap, the present study investigates the degradation behavior of GX130CrSi29 grate bars retrieved from a full-scale biomass-fired reciprocating grate furnace operating with rubberwood chips. A practical failure-analysis approach is applied by integrating macroscopic inspection with cross-sectional field-emission scanning electron microscopy (FE-SEM) and energy-dispersive X-ray spectroscopy (EDS), including elemental mapping and line-scan analysis. Rather than relying on laboratory corrosion

simulations, the analysis is based on service-exposed components operating under real industrial conditions. Although crystallographic phase identification is beyond the scope of this work, the observed morphologies and elemental distributions enable interpretation of the dominant degradation mechanisms when evaluated in the context of established biomass corrosion theories [17–22].

The contribution of this work is threefold. First, it provides microstructural evidence of multilayer degradation features in grate bars retrieved from an operating biomass furnace, thereby linking observed corrosion morphology with biomass-specific ash chemistry and furnace exposure conditions. Second, the study interprets the degradation pathway by integrating SEM/EDS observations with established theories of chlorine-assisted active oxidation and alkali–silicate fluxing in biomass combustion environments. Third, the observed non-uniform section loss is discussed within a conceptual framework that couples thermochemical corrosion with flow-assisted removal of corrosion-weakened surface layers, providing a plausible explanation for the irregular degradation patterns frequently observed in industrial grate systems.

Although the proposed framework is interpretive rather than predictive, the findings help clarify how biomass-specific ash chemistry and furnace operating conditions influence grate degradation behavior under full-scale operating conditions. The results therefore provide practical insight for grate material selection, operational management, and corrosion mitigation strategies in biomass-fired power generation systems.

2. Materials and methods

2.1. Industrial furnace description, fuel characteristics, and material verification

The investigated grate bars were retrieved from a full-scale biomass-fired reciprocating grate furnace operating at a nominal electrical capacity of 9.9 MW. The plant utilizes para-rubber woodchips as the primary fuel and is representative of very small power producer (VSPP) biomass power plants widely deployed in Southeast Asia (Fig. 1). Such facilities typically operate under continuous base-load conditions and are characterized by the combustion of alkali-rich agricultural and woody biomass fuels.

The furnace is divided along the grate length into four characteristic zones—drying, devolatilization, high-temperature combustion, and burnout—resulting in pronounced spatial gradients in temperature, oxygen availability, radiative heat flux, and alkali-vapor concentration across the grate surface (Fig. 1). These gradients impose highly non-uniform thermal and chemical exposure on grate components, particularly at flame-facing regions and locations subjected to primary-air injection from the grate nozzles. The associated thermal loading and localized air-flow effects discussed in this study are interpreted based on typical operating conditions reported in the literature for industrial biomass grate furnaces rather than on direct in-situ measurements. Similar sensitivity of wall heat flux and near-wall transport processes under reacting-flow conditions has been reported in recent studies of wall-bounded heat transfer and surface-flow interactions [23,24].

Representative fuel properties of the para-rubber woodchips obtained from routine plant operation are summarized in Table 1, including proximate and ultimate analyses. The fuel is characterized by moderate moisture content and significant concentrations of alkali-related elements. The corresponding ash composition is presented in Table 2, revealing high contents of CaO and K_2O together

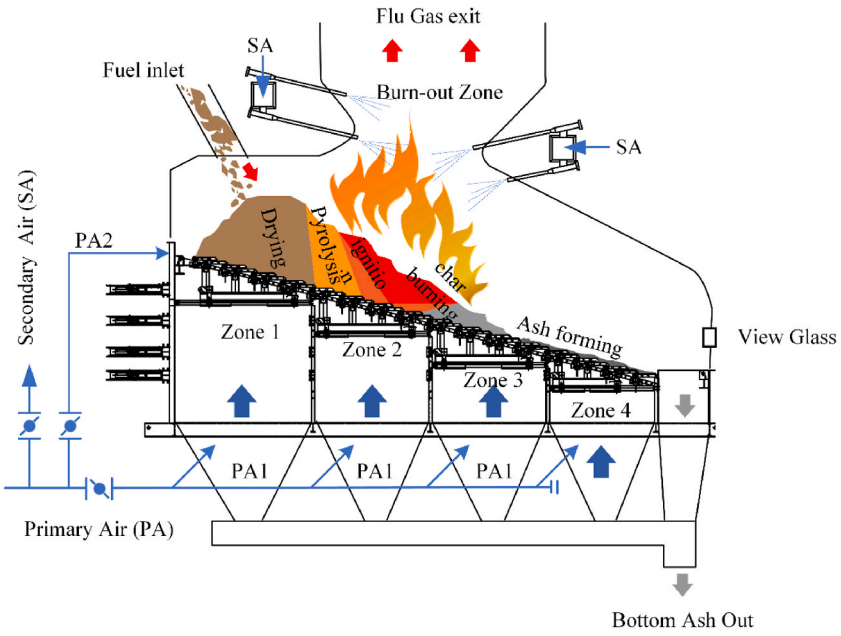

Fig. 1. Schematic diagram and representative image of the biomass-fired reciprocating grate furnace, illustrating the main combustion zones and the locations from which failed grate bars were retrieved.

Table 1
Chemical-physical parameters and corresponding reference methods.

Description	Unit	woodchip
Moisture result (EN 14774)		
Nominal moisture content:	wt.% (db)	30.00
Ash content: (EN 14775):	wt.% (db)	Nom. 1.0 – 2.0
	wt.% (db)	Max. 3.0
Volatile matter (EN 15148):	wt.% (db)	Min. 75
Carbon, C (EN 15104):	wt.% (db)	max. 42.00
Hydrogen, H (EN 15104):	wt.% (db)	max. 5.16
Nitrogen, N (EN 15104):	wt.% (db)	max. 0.50
Oxygen, O (EN 15104):	wt.% (db)	max. 40.69
Sulfur, S (EN 15289):	wt.% (db)	max. 0.07
Chlorine, Cl (EN 15104):	wt.% (db)	max. 0.01

with substantial SiO_2. This ash chemistry indicates a strong tendency for the formation of alkali–silicate-rich deposits with relatively low softening and melting temperatures, which are known to promote aggressive thermochemical interaction with metallic grate materials under biomass-fired conditions [1,3,17,21].

Under full-load operation, the boiler produces approximately 45 t/h of superheated steam at a pressure of 68 bar, with a feedwater inlet temperature of about 130 °C. The outlet steam temperature reaches approximately 520 °C, and the overall boiler efficiency is around 87.6%, corresponding to a fuel-feed rate of approximately 16.05 t/h. These operating parameters are typical of industrial VSPP biomass plants and result in sustained high thermal input together with continuous release of alkali-bearing ash species during long-term operation [4,2,3,5–8].

The failed grate bars analyzed in this study were extracted from the high-temperature combustion zone, which represents the most severe exposure region within the furnace (Fig. 1). Grate components in this region are exposed to intense flame radiation, hot flue gases, and localized air flow from primary-air nozzles, together with deposition of alkali-rich ash particles and vapors. Typical grate-surface temperatures in this zone are reported to range from approximately 800 to 1100 °C in industrial biomass grate furnaces operating under comparable conditions [2,3,5–8]. At such temperatures, ash softening, alkali–chloride volatilization, and the formation of low-melting alkali–silicate compounds are promoted, thereby enhancing thermochemical interactions between deposits and metallic grate materials [17–21].

Prior to microstructural and chemical characterization of the failed components, the alloy composition of unused grate bars from the same production batch was verified by optical emission spectrometry (OES), as shown in Fig. 2. The measured elemental concentrations, summarized in Table 3, confirm that the grate bars conform to the DIN GX130CrSi29 specification. This verification was performed solely to ensure material compliance and to exclude compositional deviation as a contributing factor to the observed degradation.

2.2. Retrieval of failed grate bar fragments and macroscopic inspection

Failed grate bar fragments were retrieved during scheduled maintenance from representative locations along the grate surface in order to capture variations in thermal, chemical, and flow-related exposure within the furnace. Sampling focused on regions exhibiting pronounced surface degradation, slag adhesion, and section loss, which are typically associated with prolonged exposure to elevated thermal loading, primary-air injection, and alkali-rich combustion products in industrial biomass grate furnaces. The selected specimens represent typical damage patterns observed during routine maintenance inspections of the grate system. The sampling locations and retrieval procedure are illustrated schematically in Fig. 3(a–d).

Three representative specimens were selected for detailed investigation to reflect different local exposure conditions along the grate surface:

Table 2
Ash analysis (ASTM D3682-01, ASTM D5016-08).

Description	Unit	woodchip
Silicon Dioxide (SiO_2)	wt.%	9.09
Aluminum oxide (Al_2O_3)	wt.%	2.14
Iron oxide (Fe_2O_3)	wt.%	1.25
Calcium oxide (CaO)	wt.%	35.77
Magnesium oxide (MgO)	wt.%	8.91
Sodium oxide (Na_2O)	wt.%	1.13
Potassium oxide (K_2O)	wt.%	27.04
Titanium oxide (TiO_2)	wt.%	9.63
Manganese oxide (Mn_3O_4)	wt.%	0.89
Sulfur trioxide (SO_3)	wt.%	0.23
Phosphorus pentoxide (P_2O_5)	wt.%	3.36

Fig. 2. Photograph of a representative grate bar specimen used for optical emission spectrometry (OES) to verify the bulk chemical composition prior to microstructural analysis.

Table 3
Chemical composition of the grate-bar material (DIN GX130CrSi29) determined by optical emission spectrometry (OES) and compared with the standard composition range.

Element	Standard Min	Standard Max	OES Sample 1	OES Sample 2
C	1.20	1.40	1.29	1.30
Si	1.00	2.50	1.77	1.72
Mn	0.50	1.00	0.98	0.77
P	–	0.035	0.032	0.032
S	–	0.030	0.010	0.010
Cr	27.00	30.00	28.62	28.08
Mo	–	0.50	0.50	0.50
Ni	–	1.00	0.012	0.010

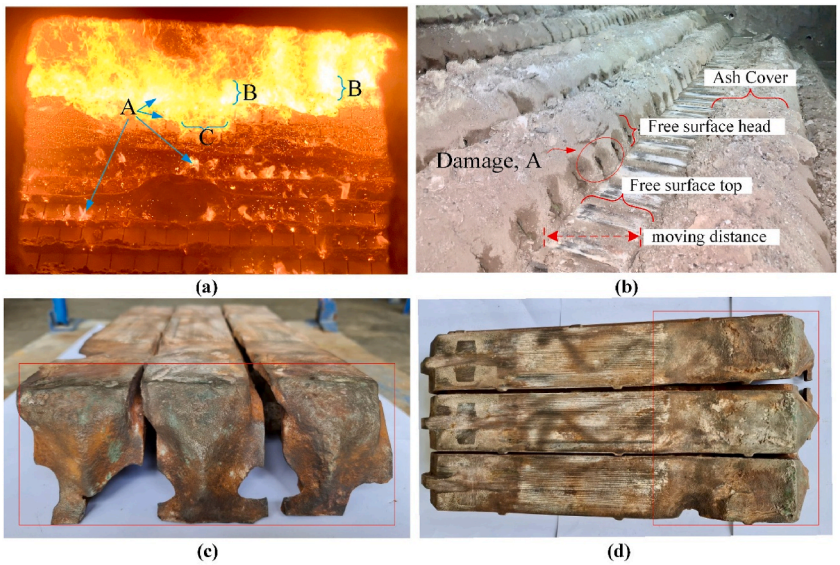

Fig. 3. (a) Over-grate view of the combustion zone showing flame-front position, ash coverage, and exposed grate surfaces used to identify sampling locations. (b) Field removal of failed grate bars showing free-surface regions, ash-covered zones, and localized damage at the leading edge. (c–d) Extracted grate specimens after cooling, highlighting severe material loss at the head region and progressive degradation along the grate motion direction.

2.2.1. Sample A – leading-edge fragment

A fragment detached from the front (leading-edge) region of the grate bar, where exposure to flame radiation, elevated surface temperatures, and alkali-salt deposition is expected to be most severe. This region is commonly considered thermally and chemically aggressive due to direct proximity to the combustion flame and higher local gas velocities associated with primary-air injection.

2.2.2. Sample B – mid-grate fragment

A fragment originating from the mid-grate region, corresponding to areas primarily subjected to alkali vapor impingement and ash deposition, with comparatively lower direct radiative loading and reduced local air-flow intensity than the leading-edge region.

2.2.3. Sample C – leading-edge severe damage

A second specimen from the leading-edge region was selected to obtain a more controlled and representative cross-section for detailed microstructural and elemental analysis, particularly in zones exhibiting advanced material loss and scale detachment.

All retrieved fragments were documented by photography and examined using a stereomicroscope prior to further preparation. Macroscopic features including surface melting, oxide scaling, slag adhesion, non-uniform metal thinning, crack networks, and localized material loss were recorded in order to establish the overall damage morphology and guide subsequent microstructural characterization. Representative macroscopic observations are presented in section 3.1.

2.3. Preparation of cross-sectional specimens

Cross-sectional specimen preparation was tailored to the highly degraded and brittle condition of the failed grate bars in order to preserve fragile corrosion layers and deposit structures formed during service. The overall preparation workflow is summarized in Fig. 4.

For Samples A and B, which had already fractured during service, gentle mechanical separation was used to expose cross-sections approximately perpendicular to the primary degradation direction. This approach minimized additional thermal and mechanical damage and helped preserve delicate multilayer corrosion features developed during operation, including the outer ash/slag adhesion layer, porous iron-rich oxide scales, chromium-enriched inner oxide regions, chromium-depleted metal zones, and areas of internal oxidation. The exposed fragments were subsequently mounted in epoxy resin to provide mechanical support during subsequent metallographic preparation.

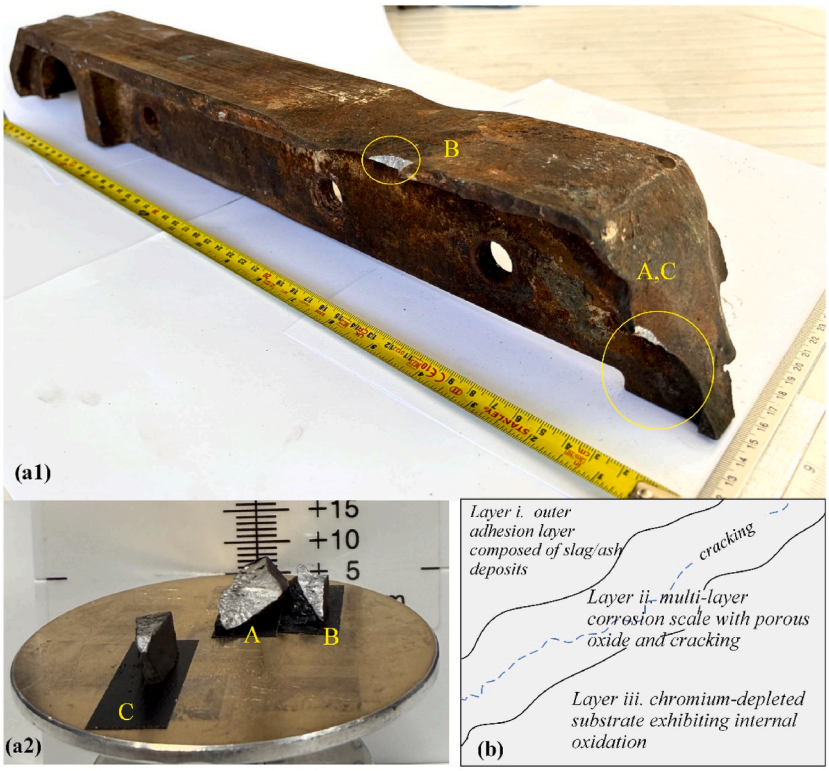

Fig. 4. (a) Preparation of failed grate-bar fragments for cross-sectional analysis: Sample A – leading-edge fragment (severe degradation), Sample B – mid-grate fragment (moderate degradation), and Sample C – leading-edge fragment with severe damage prepared by controlled cutting. (b) Schematic cross-sectional orientation used for SEM imaging and EDS elemental analysis.

For Sample C, a cleaner and more planar cross-section was required to facilitate SEM/EDS line-scan and elemental mapping analyses. The specimen was therefore sectioned using a low-speed diamond cutting wheel under continuous coolant flow in order to minimize heat generation, mechanical deformation, and potential secondary oxidation. After sectioning, the specimen was mounted in epoxy and subjected to standard metallographic preparation procedures.

Grinding was carried out sequentially using silicon carbide (SiC) abrasive papers with progressively finer grit sizes (typically 240, 400, 600, 800, and 1200 grit) to obtain a flat cross-sectional surface. The specimens were subsequently polished using diamond suspensions with particle sizes of approximately 3 μm and 1 μm to produce a smooth and damage-free surface suitable for high-resolution SEM observation and compositional analysis.

Following polishing, all specimens were ultrasonically cleaned in ethanol to remove residual polishing debris prior to microscopic examination. The prepared cross-sections clearly revealed the stratified architecture of the degraded material, including surface deposits, multilayer corrosion scales, the oxide–metal interface, and the underlying substrate microstructure. These prepared sections served as the basis for the microstructural and chemical analyses presented in Sections 3.1–3.3.

2.4. Field emission scanning electron microscopy (FE-SEM) and energy-dispersive X-ray spectroscopy (EDS)

Microstructural and compositional characterization of the failed grate bars was conducted using field-emission scanning electron microscopy (FE-SEM) combined with energy-dispersive X-ray spectroscopy (EDS). The FE-SEM/EDS technique was employed primarily as a diagnostic tool to examine degradation features relevant to failure analysis under industrial biomass-firing conditions, rather than as an exhaustive materials-characterization procedure. SEM observations directly reveal corrosion morphology, while EDS analyses provide elemental distributions that support interpretation of the degradation mechanisms.

Both secondary electron (SE) and backscattered electron (BSE) imaging modes were used to examine surface morphology, layer continuity, porosity, cracking, and compositional contrast across the corrosion layers. Observations were systematically focused on degradation features commonly reported in biomass-fired environments, including (i) outer ash or slag adhesion layers, (ii) multilayer corrosion scales, (iii) oxide–metal interface morphology, (iv) chromium-depleted substrate regions, and (v) internal oxidation and subsurface damage.

To evaluate spatial variations in degradation behavior, comparative analyses were performed between specimens retrieved from the leading-edge regions (Samples A and C) and the mid-grate region (Sample B). SEM images were acquired over a magnification range sufficient to capture both overall layer architecture and fine-scale features such as oxide fragmentation, pore networks, and microcracking. Representative cross-sectional micrographs illustrating position-dependent degradation characteristics are presented in Section 3.

EDS analyses, including point analysis, line scanning, and elemental mapping, were conducted to identify elemental distributions across the corrosion layers and substrate. The spatial distributions of Fe, Cr, O, K, Cl, S, and Si were examined in order to evaluate compositional variations associated with different degradation regions. Line-scan profiles were used to identify chromium-depleted zones adjacent to the oxide–metal interface and to assess the penetration of alkali and silicon species into the corrosion layers. Elemental mapping further enabled visualization of chemically distinct regions that may correspond to alkali-rich deposits and corrosion products formed under biomass-firing conditions.

It should be noted that quantitative phase identification was not performed in the present study. Consequently, the SEM/EDS results are interpreted in conjunction with morphological evidence and established corrosion mechanisms reported in the biomass combustion literature, rather than being used as direct confirmation of specific crystalline phases.

2.5. Integrated Microstructural–Chemical framework for failure mechanism determination

The failure mechanisms of the grate bars were interpreted using an integrated microstructural–chemical analysis framework that combines macroscopic damage observations, cross-sectional microstructural features, and elemental distributions obtained from FE-SEM and EDS analyses. These observations were evaluated together with thermochemical corrosion mechanisms established in the literature for biomass-fired combustion environments. The framework aims to systematically link observable degradation features to dominant degradation processes occurring under real full-scale industrial operating conditions, rather than to establish a predictive corrosion model.

Specifically, the failure-mechanism interpretation integrates the following complementary sources of evidence:

1. macroscopic inspection of failed grate bar surfaces and localized damage morphology.
2. cross-sectional corrosion-layer architecture revealed by FE-SEM imaging.
3. compositional contrast and morphological features observed using secondary electron (SE) and backscattered electron (BSE) imaging modes.
4. elemental distributions obtained from EDS point analyses, line scans, and elemental mapping.
5. established degradation mechanisms reported in the literature for biomass combustion environments, including chlorine-assisted active oxidation, alkali-driven molten silicate fluxing, sulfate-related interactions, and thermomechanical effects.

The multilayer corrosion architecture was consistently observed across the analyzed specimens, including both leading-edge samples (A and C) and the mid-grate sample (B). This repeatable structural pattern supports the interpretation that the observed degradation features reflect systematic thermochemical processes occurring in the furnace environment rather than isolated or

specimen-specific anomalies.

Among these sources of evidence, chromium depletion near the oxide–metal interface and the presence of chlorine-bearing deposits provide the most direct indicators of chlorine-assisted active oxidation. In contrast, the distribution of potassium- and silicon-enriched regions within adhesion and corrosion layers serves as supporting evidence for the involvement of alkali-rich deposits and possible molten silicate fluxing. Macroscopic damage morphology and corrosion-layer architecture provide contextual information on the spatial progression of degradation along the grate surface.

Within this framework, chromium-depleted zones adjacent to the oxide–metal interface were therefore interpreted as microchemical indicators consistent with chlorine-assisted active oxidation. Iron- and chromium-enriched oxide regions observed near the oxide–metal interface were evaluated in the context of mixed iron–chromium oxide formation commonly reported for high-temperature corrosion of chromium-containing alloys in biomass-fired systems. Similarly, potassium- and silicon-enriched regions within the outer corrosion layers were interpreted as evidence of alkali-bearing deposits that may contribute to fluxing and destabilization of protective oxide layers.

Direct crystallographic phase identification was not performed in the present study. Consequently, the proposed corrosion products and degradation pathways are based on the combined interpretation of microstructural morphology, elemental distributions, and comparison with well-established degradation mechanisms reported in the literature. The integrated SEM/EDS-based framework applied here follows general failure-analysis methodologies previously reported for grate components, while extending them to explicitly consider the alkali-rich and chloride-bearing chemistry characteristic of biomass combustion environments, which differs significantly from iron-ore sintering and fossil-fuel-fired systems.

Overall, the methodology emphasizes failure diagnosis based on microstructural and chemical evidence obtained from service-exposed components under full-scale operating conditions, consistent with the objectives of practical industrial case studies in thermal and combustion engineering.

3. Results

3.1. Macroscopic damage characteristics of failed grate bars

Three representative fragments of failed grate bars (Samples A–C), shown in Fig. 5, were collected from distinct furnace locations as described in Section 2.2. The specimens exhibit varying degrees of degradation, reflecting differences in local thermal loading and exposure to ash-derived corrosive species along the grate.

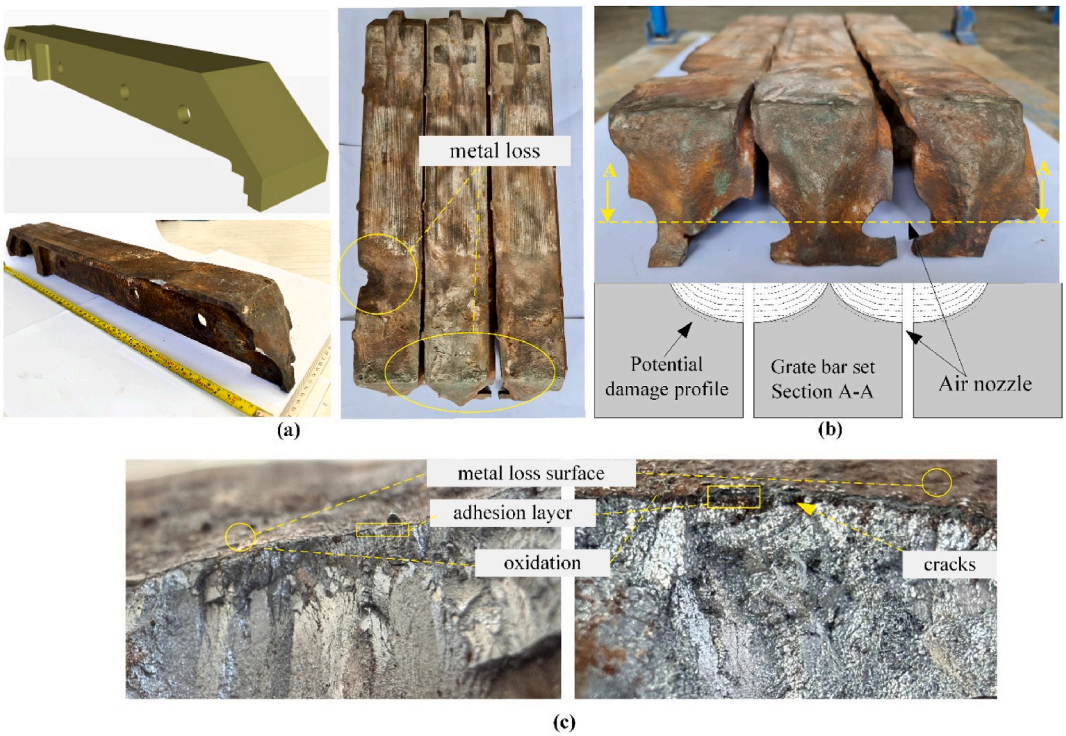

Fig. 5. Macroscopic morphology of failed grate bars: (a) Overall geometry of extracted bars with reference CAD profile for comparison. (b) Severe leading-edge degradation characterized by metal loss, deformation, and localized melting. (c) Surface oxidation, slag adhesion, and crack formation observed along the upper surface of the grate bar.

The nominal thickness of the grate-bar head region in the original design is approximately 10–15 mm based on the geometry of unused grate bars from the same production batch. Macroscopic inspection of the retrieved fragments indicates substantial section loss at flame-facing regions. In the most severely degraded areas of the leading-edge specimens (Samples A and C), the remaining metal thickness was estimated to be approximately 4–6 mm, corresponding to an approximate section reduction of about 50–60%. In contrast, the mid-grate specimen (Sample B) retained a larger fraction of the original cross-section, with remaining thickness typically in the range of approximately 7–10 mm, corresponding to an estimated section reduction of roughly 20–35%. These estimates were obtained through direct macroscopic observation and comparison with the original grate-bar geometry.

Sample A, retrieved from the leading-edge region, shows the most severe damage, characterized by extensive metal loss, localized surface melting, and thick slag adhesion. Sample B, originating from the mid-grate region, exhibits comparatively moderate degradation with thinner slag accumulation and shallower section loss. Sample C, also taken from the leading-edge region but prepared using controlled cutting, displays damage characteristics similar to Sample A, indicating that the most aggressive degradation occurs consistently at the flame-facing front regions of the grate.

Despite differences in severity, all specimens share several common macroscopic features, including pronounced surface roughening, oxide scaling, resolidified slag adhesion, crack networks associated with thermal cycling, and non-uniform thinning of flame-facing surfaces. These recurring damage patterns suggest that grate degradation is primarily associated with the thermochemical exposure environment of the furnace rather than with localized material defects or compositional non-conformance.

3.2. *Multilayer corrosion architecture revealed by cross-sectional SEM observations*

Low- and high-magnification cross-sectional SEM images of Samples A–C reveal a reproducible multilayer corrosion architecture across all investigated grate bars, with position-dependent variations in layer thickness and morphology (Fig. 6). The structural sequence of the corrosion layers and the compositional contrast between them are further illustrated in the corresponding cross-

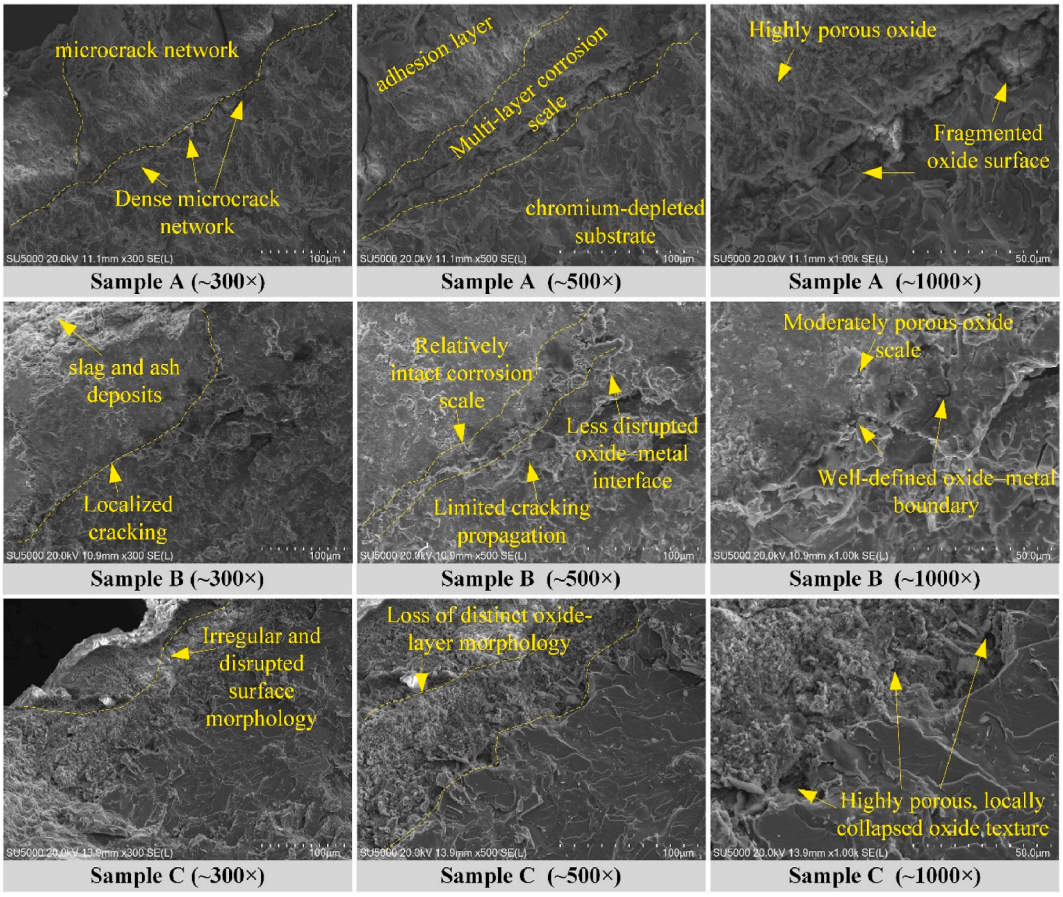

Fig. 6. Representative cross-sectional FE-SEM images showing position-dependent corrosion morphology of GX130CrSi29 grate bars. Sample A (leading-edge region) exhibits a thick multilayer corrosion scale, a degraded Cr-enriched inner oxide, and a Cr-depleted substrate with highly porous Fe-rich outer oxide. Sample B (mid-grate region) shows thinner deposits and a more continuous corrosion-layer structure. Sample C (leading-edge severe exposure) displays disrupted corrosion layers and locally collapsed porous oxide structures indicative of advanced degradation.

sectional images shown in Fig. 7.

3.2.1. Observed morphology

Three characteristic regions are consistently visible in the SEM cross-sections:

1. Outer adhesion layer

The outermost region consists of a heterogeneous adhesion layer containing slag particles, ash deposits, and fused material attached to the grate surface. As illustrated in Fig. 6, this layer appears thicker in the leading-edge samples (Samples A and C) and noticeably thinner in the mid-grate sample (Sample B), indicating spatial differences in ash-deposition intensity and local thermal exposure.

2. Multilayer corrosion scale

Beneath the adhesion layer, a multilayer corrosion scale is present, consisting of a porous outer oxide and a comparatively denser inner oxide layer. The structural distinction between these layers and their compositional contrast are clearly visible in the BSE images shown in Fig. 7.

3. Subsurface degradation zone

At the oxide–metal interface, the underlying substrate exhibits localized subsurface degradation, including internal oxidation features and grain-boundary attack extending into the metal matrix. The depth of this subsurface degradation is most pronounced in the leading-edge specimens.

3.2.2. Interpretation

These structural features are broadly consistent with corrosion architectures reported for high-temperature degradation of chromium-containing alloys in biomass combustion environments. The thicker adhesion layer and more porous oxide scales observed in the leading-edge specimens suggest more severe exposure conditions at flame-facing regions of the grate. Despite differences in damage intensity, the same multilayer corrosion sequence is observed in all specimens, providing a consistent structural basis for subsequent interpretation of the degradation mechanisms.

3.3. Elemental distribution and chemical evidence from EDS analyses

EDS line-scan profiles and elemental maps provide elemental distribution information associated with the corrosion layers identified in the SEM observations. Representative line-scan profiles are shown in Fig. 8, while the corresponding elemental maps are

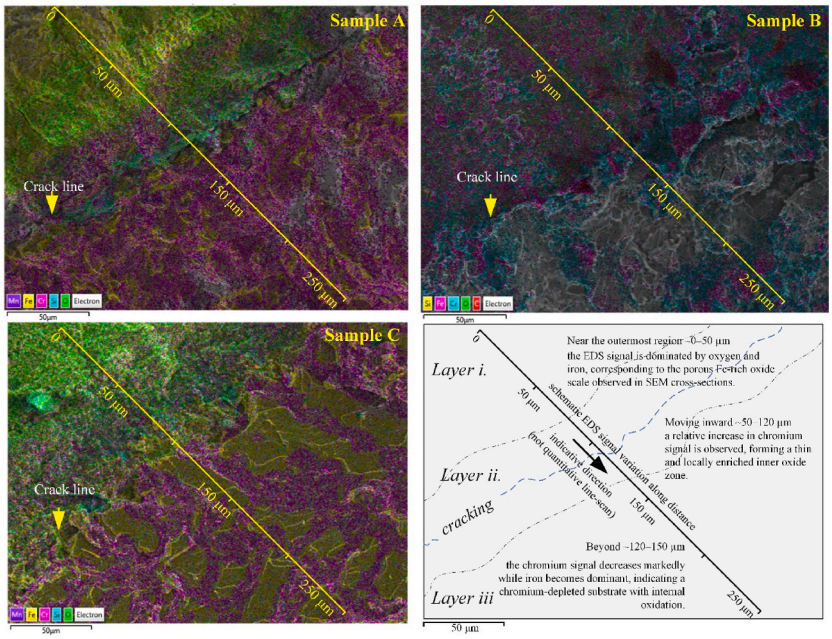

Fig. 7. Cross-sectional SEM images and corresponding EDS elemental maps illustrating the multilayer corrosion architecture of the GX130CrSi29 grate bars, consisting of alkali-rich surface deposits, a porous Fe-rich outer oxide, a degraded Cr-enriched inner oxide, and a Cr-depleted substrate.

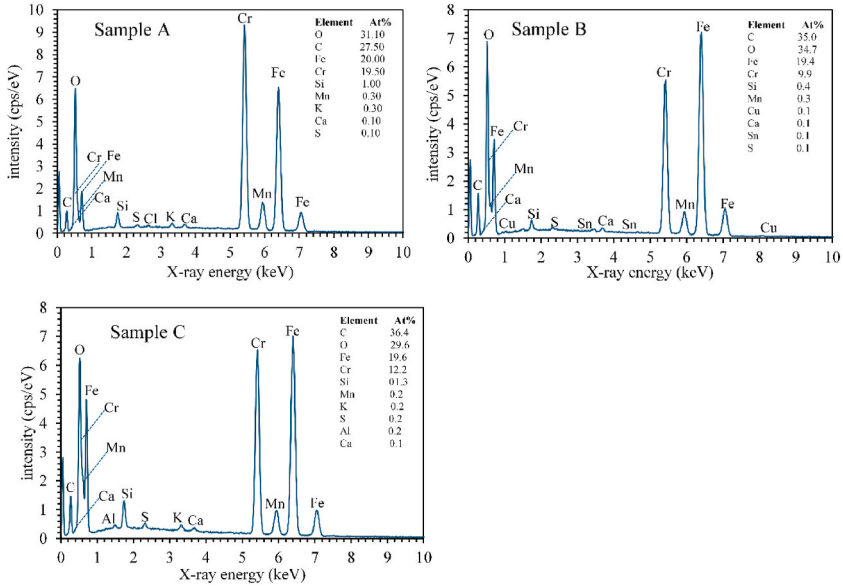

Fig. 8. EDS line-scan profiles obtained across the corrosion layers of Samples A–C, showing elemental gradients from alkali-rich surface deposits through the Fe-rich outer oxide and degraded Cr-enriched inner oxide toward the Cr-depleted substrate.

presented in Fig. 9.

Across all investigated samples, the outer adhesion layer exhibits relatively low Fe and Cr signals together with enrichment of K, Si, Ca, and S. These elemental distributions indicate the presence of biomass-derived ash deposits containing alkali and silicate species.

Within the corrosion scale, the outer oxide layer is dominated by Fe with only limited chromium contribution. Moving toward the oxide–metal interface, a relative increase in chromium signal intensity is observed within an intermediate oxide region corresponding to a degraded Cr-enriched inner oxide. However, chromium concentrations remain substantially lower than the nominal alloy composition of GX130CrSi29, suggesting progressive chromium depletion during service exposure of the grate bars.

Closer to the metal substrate, oxygen penetration is observed in combination with chromium depletion and trace alkali species. These compositional gradients are consistent with inward oxygen diffusion and interaction between corrosion products and biomass-derived ash components. The elemental distributions therefore provide chemical context supporting the multilayer corrosion architecture observed in the SEM images.

3.4. Integrated SEM/EDS evidence of degradation features

High-magnification SEM imaging combined with localized EDS analysis (Fig. 10) reveals pronounced chemical and morphological heterogeneity within the adhesion layer and upper corrosion scale.

Three representative microstructural features are identified:

1. **Iron-rich oxide regions** (Fig. 10(a))

These regions exhibit elongated or plate-like morphologies enriched in Fe and O with minor alkali contributions.

2. **Porous oxide textures** (Fig. 10(b))

These areas contain diffuse alkali distributions and extensive porosity within the oxide scale.

3. **Glassy alkali-rich regions** (Fig. 10(c))

These compact regions show strong enrichment in Ca and K together with Fe and O, suggesting the presence of alkali-rich glassy phases formed during high-temperature interaction between ash deposits and the metal surface.

Collectively, the SEM and EDS observations indicate that the adhesion layer and corrosion scale are chemically and morphologically heterogeneous, consisting of both oxidation-derived iron-rich oxides and alkali-rich deposit phases. Such heterogeneity reflects spatial and temporal variations in temperature, ash chemistry, and local oxygen potential within the biomass combustion environment.

Overall, the results indicate that degradation of GX130CrSi29 grate bars in the investigated furnace is associated with the combined effects of alkali-rich ash deposition, unstable oxide growth, chromium depletion, and molten-phase interactions, rather than uniform

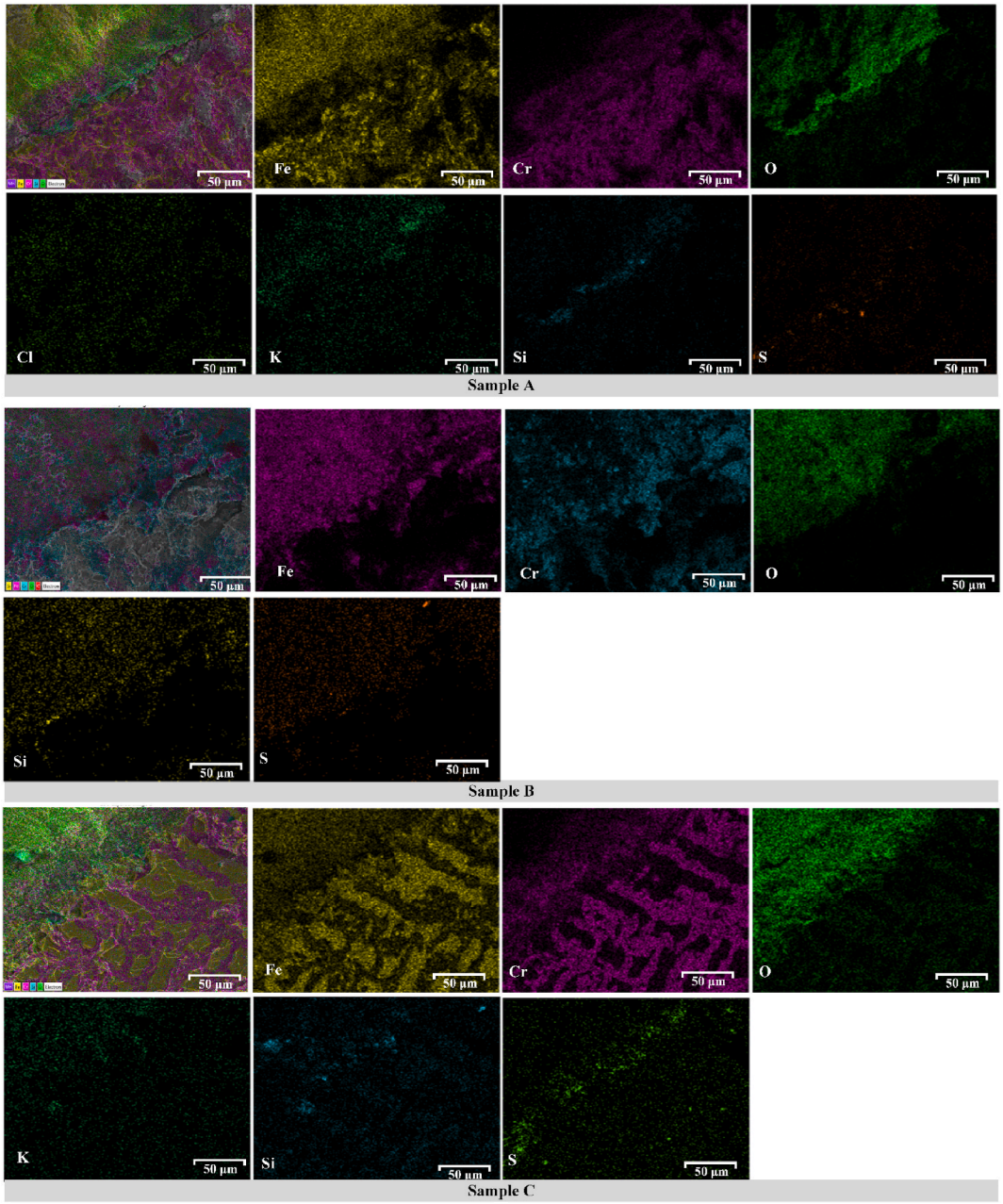

Fig. 9. EDS elemental maps of corrosion layers in Samples A–C illustrating the spatial distributions of Fe, Cr, O, K, Cl, Si, and Ca. The maps highlight alkali–silicate deposits, chromium depletion near the oxide–metal interface, and oxygen penetration into the substrate.

high-temperature oxidation alone.

4. Discussion

4.1. Determination of the dominant degradation mechanism under biomass-fired conditions

Based on the combined macroscopic observations, cross-sectional microstructural features, and SEM/EDS-derived elemental distributions obtained from Samples A–C, degradation of GX130CrSi29 grate bars operating in the investigated biomass-fired furnace appears to be governed primarily by a synergistic thermochemical corrosion process. The corrosion pathway observed in all examined specimens indicates that multiple interacting mechanisms contribute to degradation under biomass-fired conditions.

Within this hierarchy of processes, chlorine-assisted active oxidation is interpreted as the initiating mechanism, while

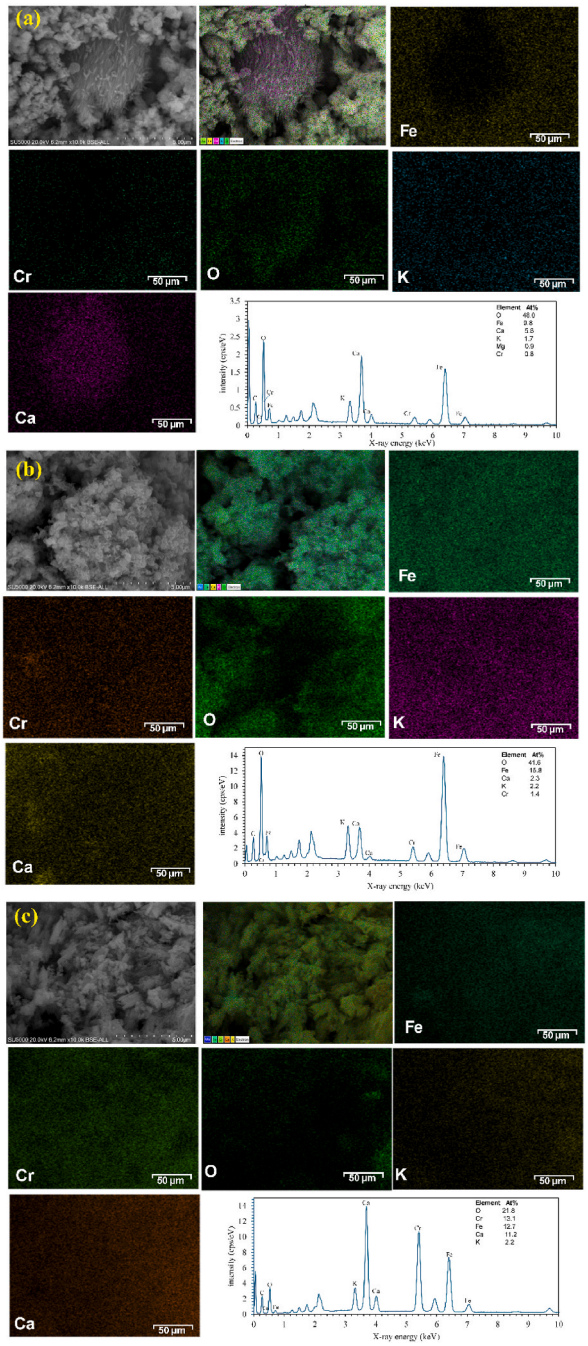

Fig. 10. High-magnification SEM images with corresponding EDS elemental maps showing representative corrosion textures within the adhesion layer and corrosion scale: (a) Fe-rich oxide regions containing minor alkali species, (b) porous Fe-rich oxide scale with dispersed alkali elements, and (c) alkali- and Ca-enriched glassy corrosion products.

alkali–silicate fluxing acts primarily as an accelerating process that intensifies corrosion once the protective oxide barrier has been destabilized. Although the severity of degradation varies with furnace position, the observed corrosion-layer sequence and microstructural features remain consistent across all analyzed specimens, indicating that degradation is primarily controlled by the furnace environment rather than by localized material defects or alloy non-conformance.

A key observation supporting this interpretation is the destabilization of the chromium-rich protective barrier. High-chromium cast steels rely on the formation of a continuous chromium-enriched oxide layer to resist high-temperature oxidation. In the present study, SEM cross-sections consistently reveal only a thin and locally discontinuous Cr-enriched inner oxide accompanied by pronounced chromium depletion in the underlying substrate. EDS line-scan profiles further show that chromium concentrations near the

oxide–metal interface remain significantly below the nominal alloy composition, suggesting progressive chromium consumption during service.

Such chromium depletion is widely associated with biomass combustion environments containing alkali and chlorine species, which destabilize chromia-based protective layers through chlorine-assisted active oxidation cycles [17,18]. In these cycles, chlorine-bearing species—present either as HCl in the gas phase or as alkali chlorides within ash deposits—react at or near the oxide–metal interface to form volatile metal chlorides. Subsequent oxidation of these chlorides away from the interface regenerates chlorine, sustaining a cyclic corrosion process. The presence of potassium- and chlorine-enriched regions within the adhesion layers provides microchemical evidence consistent with the operation of this mechanism under the investigated furnace conditions. Similar degradation behavior of chromium-containing alloys has been widely reported in biomass- and waste-fired systems as well as under controlled chlorine-containing atmospheres [14,20].

Once the chromium-based protective barrier becomes destabilized, oxidation proceeds predominantly through the formation of iron-rich oxides. SEM observations consistently reveal a thick and porous iron-rich outer oxide scale characterized by extensive cracking and void networks, particularly in the leading-edge samples (Samples A and C). These features indicate repeated oxide growth, cracking, and local detachment during service exposure. Although crystallographic phase identification was not performed in this study, the observed morphology and scale characteristics are consistent with iron-oxide-dominated corrosion layers reported in alkali- and chloride-affected high-temperature environments [17,18,20].

In parallel with oxidation processes, alkali-rich biomass ash contributes to accelerated degradation. SEM/EDS mapping reveals strong enrichment of potassium, silicon, and calcium within the adhesion layers together with evidence of penetration into the corrosion scale along pores and cracks. The glassy and partially fused morphology of these deposits, particularly in the leading-edge samples, suggests melting and resolidification during service exposure. Molten or semi-molten alkali–silicate phases can enhance degradation by dissolving protective oxides, increasing ionic transport through the scale, and weakening oxide adherence, thereby facilitating spallation and renewed oxidation [21]. In this context, alkali–silicate fluxing acts primarily as an accelerating process that intensifies corrosion once active oxidation has disrupted the protective oxide barrier.

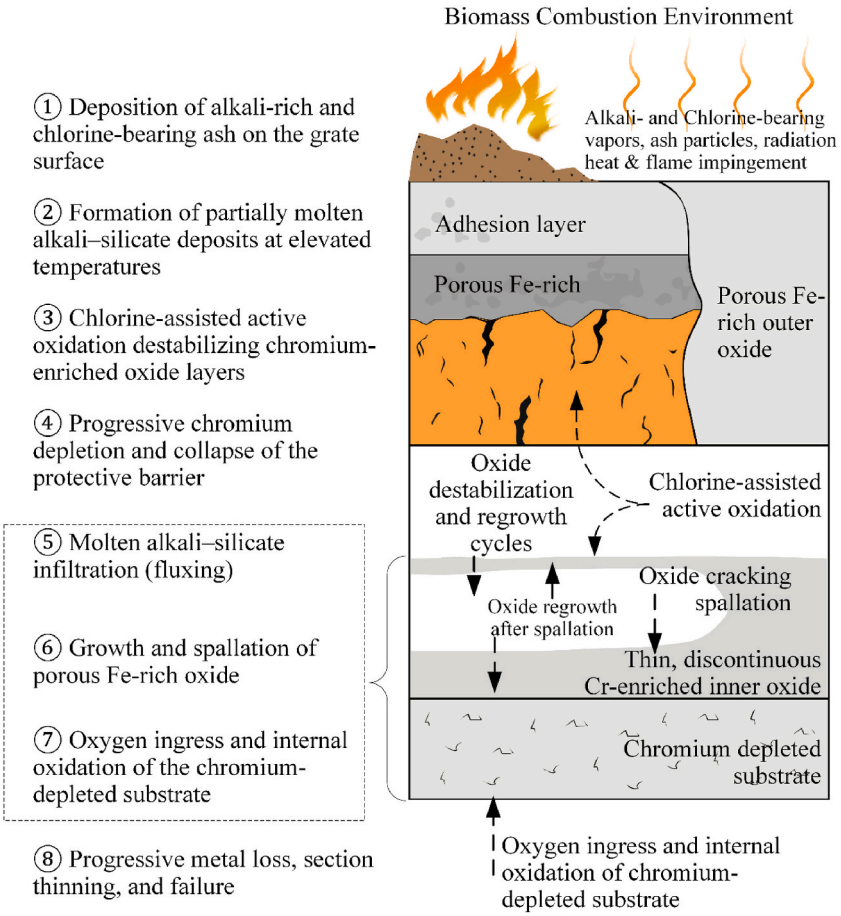

Fig. 11. Proposed integrated degradation sequence for GX130CrSi29 grate bars under rubberwood-fired biomass combustion, illustrating ash deposition, chlorine-assisted active oxidation, formation of Fe-rich oxide scales, alkali–silicate fluxing, internal oxidation, and progressive section loss.

Subsurface degradation provides additional evidence supporting this interpretation. Oxygen penetration and internal oxidation fronts are observed in all samples, with the greatest penetration depths occurring in the leading-edge regions. Internal oxidation and grain-boundary attack are interpreted as downstream consequences of chromium depletion and porous oxide development, which reduce the alloy's ability to suppress oxygen ingress. These subsurface features can compromise mechanical integrity and promote crack initiation and propagation under the combined thermal and mechanical loading experienced during grate operation [25].

Although the same degradation mechanisms operate throughout the grate system, their severity is strongly modulated by local thermochemical exposure conditions. Leading-edge locations experience higher thermal loading, direct flame exposure, and more intense alkali-laden deposition, resulting in the most severe degradation. In contrast, mid-grate regions undergo similar processes at reduced intensity. This spatial dependence indicates that local furnace operating conditions govern corrosion severity [4,26,3,6–8].

4.2. Proposed integrated failure sequence

Based on the degradation features identified in Sections 3.1–3.4, the failure of GX130CrSi29 grate bars under rubberwood-fired biomass combustion can be interpreted as progressing through an integrated sequence of thermochemical processes. The proposed sequence is schematically illustrated in Fig. 11.

The exact time scale of each stage cannot be determined from the present failure-analysis data; however, the sequence likely develops progressively throughout the service life of the grate bars under sustained biomass-fired operating conditions.

The degradation pathway can therefore be described by the following conceptual sequence:

1. Deposition of biomass-derived ash species

Alkali-rich and siliceous ash particles containing chlorine-bearing species deposit on the grate surface during combustion.

2. Initiation of chlorine-assisted active oxidation

Chlorine-bearing species promote active oxidation reactions at or near the oxide–metal interface, progressively destabilizing chromium-enriched protective oxide layers [17,18,20].

3. Development of a porous iron-rich oxide scale

Following disruption of the protective chromia barrier, oxidation proceeds primarily through the formation of iron-rich oxide layers characterized by porosity, cracking, and repeated local spallation.

4. Fluxing-assisted destabilization of corrosion layers

Alkali–silicate-rich material penetrates the porous corrosion scale through cracks and void networks, promoting dissolution of oxide layers and weakening scale adherence through molten or semi-molten fluxing processes [21].

5. Subsurface oxidation and microstructural degradation

Oxygen ingress into the chromium-depleted substrate leads to internal oxidation, grain-boundary attack, and progressive weakening of the metal matrix.

6. Progressive section loss and mechanical failure

Continued corrosion and repeated removal of weakened oxide layers ultimately produce significant metal recession, localized softening at flame-facing leading edges, and eventual mechanical failure of the grate bars.

This integrated degradation sequence is consistent with biomass-induced corrosion pathways reported in the literature [17–22], while also aligning with the macroscopic damage patterns and multilayer corrosion structures observed in the analyzed grate-bar specimens.

4.3. Implications for grate design and operation under biomass firing

The degradation mechanisms identified in this study highlight the dominant influence of local thermochemical exposure on grate durability in biomass-fired furnaces. Leading-edge regions directly exposed to flame radiation and alkali-rich combustion products experience the most severe degradation, whereas regions partially shielded by the fuel bed or ash layers exhibit comparatively reduced damage. This spatial dependence suggests that physical shielding from direct thermal radiation and chemically aggressive species plays an important role in moderating grate degradation [4,26,2,3,6–8].

Ash coverage in particular can provide a beneficial protective effect. Ash layers accumulated on the grate surface may act as both a thermal and chemical barrier, reducing direct flame radiation and limiting exposure to alkali-rich gas streams. Such coverage can also moderate surface temperature fluctuations and reduce direct contact between the metallic surface and aggressive ash-derived species.

In this context, controlled ash retention can partially mitigate the thermochemical conditions responsible for active oxidation and fluxing-assisted degradation.

From a design perspective, grate geometries that promote the retention of a stable ash layer may help reduce degradation rates. Examples include the incorporation of angled ribs, surface roughness features, or grate-bar profiles that encourage ash accumulation and reduce direct line-of-sight exposure to flame radiation and high-velocity gas streams. These design approaches aim to maintain a protective ash blanket over critical regions of the grate surface.

Operational practices also play an important role in controlling local exposure conditions. Excessive removal of ash or fuel-bed material during operation may expose grate surfaces to more aggressive thermal and chemical environments. Conversely, maintaining a stable fuel bed and controlled ash coverage can reduce direct surface exposure and moderate degradation processes at critical locations [26,6,8,21].

Overall, these observations suggest that managing local thermochemical exposure through grate geometry, ash handling practices, and furnace operation can provide effective mitigation strategies. Such measures may complement material selection strategies and contribute to extending the service life of grate components in biomass-fired combustion systems.

4.4. Comparison with degradation mechanisms in iron ore sintering grate bars

The degradation behavior interpreted in the present study differs fundamentally from that reported for iron ore sintering grate bars, such as those investigated by Fan et al. [13]. Iron ore sintering environments are typically dominated by O_2–CO–CO_2 gas mixtures and Fe–Ca–Si particulates, which primarily promote oxidation and carburization processes while lacking the intense alkali–-chloride–silicate chemistry characteristic of biomass combustion systems. As a result, degradation of sintering grate bars is generally governed by oxidation, carburization, and diffusion-controlled microstructural evolution of chromium-containing alloys [13,15].

In contrast, the degradation pathway identified in the present biomass-fired system is strongly influenced by chemically aggressive ash species containing alkali metals, chlorine, and siliceous components. These species promote chlorine-assisted active oxidation and alkali–silicate-driven fluxing processes that destabilize chromium-rich protective oxides and accelerate corrosion under biomass combustion conditions [17–21]. Such chemically driven degradation mechanisms are not typically present in iron ore sintering environments.

A key distinction is therefore the role of ash-derived chemistry in controlling corrosion behavior. In biomass-fired furnaces, the combined presence of potassium, chlorine, and silicon produces aggressive thermochemical conditions that can destabilize protective oxide scales and promote repeated oxide disruption and regrowth. In contrast, sintering systems generally lack the strong alkali–-chloride interactions required to initiate active oxidation cycles.

This comparison highlights an important implication of the present study: degradation mechanisms identified for sintering grate bars cannot be directly extrapolated to biomass-fired combustion systems. The failure-analysis results obtained from service-exposed biomass grate bars therefore provide new evidence regarding biomass-specific corrosion pathways operating under real industrial conditions.

To reflect the absence of direct crystallographic phase identification in the present work, the comparison focuses on environmental drivers and mechanistic features inferred from microstructural morphology and elemental distributions rather than on specific oxide phase identification. A summary comparison between biomass-fired and sintering grate-bar degradation mechanisms is provided in Table 4.

While these dominant thermochemical mechanisms explain the origin of corrosion damage, they do not fully account for the highly non-uniform and accelerated section loss observed in service. This observation motivates the coupled corrosion–flow interpretation discussed in the following section.

4.5. Coupled thermochemical corrosion and flow-assisted removal mechanism

The degradation behavior of the grate bars observed in this study is interpreted using a coupled framework that integrates thermochemical corrosion with the removal of corrosion-weakened surface layers under furnace gas flow. The proposed framework is

Table 4
Comparison of degradation environments and mechanisms between iron ore sintering [13] and the present biomass-fired furnace (SEM/EDS-based interpretation).

Aspect	Iron Ore Sintering Grate Bars [13]	Biomass Combustion Grate Bars (This study)
Primary atmosphere	O_2–CO–CO_2 rich; redox cycling	Alkali- and chlorine-bearing flue gas; deposit-driven chemistry
Major corrosive drivers	Oxidation + carburization; Fe–Ca–Si particulates	K-, Cl-, Si-, Ca-, S-bearing deposits; active oxidation + fluxing [17–21]
Deposit character	Fe–Ca–Si dust (higher melting tendency)	Partially fused/glassy alkali–silicate-rich slag (low-melting tendency) [21]
Protective layer behavior	Chromium-enriched oxide may remain partially stable [13]	Chromium-enriched inner oxide becomes thin/discontinuous; strong Cr depletion [17–20]
Outer scale morphology	Layered oxide; relatively cohesive [13]	Porous Fe-rich outer scale; cracking and spallation–regrowth
Internal oxidation	Limited/shallow [13]	Deep oxygen ingress; grain-boundary oxidation evident
Dominant mechanism	Oxidation + carburization [13,15]	Active oxidation + molten/deposit-assisted fluxing [17–21]
Overall severity	Moderate	High to extreme at leading edge (position-dependent)

intended as a conceptual interpretation of the observed degradation patterns rather than as a calibrated predictive model. The interpretation is based on SEM–EDS observations together with typical operating conditions reported for industrial biomass grate furnaces.

Under biomass-fired conditions, alkali–chloride–silicate species originating from fuel ash promote accelerated oxidation, fluxing, and the formation of porous and mechanically weak oxide–deposit layers. SEM–EDS analyses reveal enrichment of alkali and silicon species in the outer corrosion layers. In addition, chromium depletion is observed beneath the oxide–metal interface, indicating destabilization of protective chromium-rich oxides.

In addition to thermochemical weakening of surface layers, gas-flow interaction may influence the persistence of these layers under furnace conditions. In grate-fired furnaces, localized primary-air injection and hot flue-gas flow interact with the grate surface. The flow-assisted removal mechanism proposed in this study is therefore inferred from the observed corrosion morphology and the typical operating context of industrial grate furnaces, rather than from direct measurements of local flow fields or erosion forces. Repeated detachment of porous oxide and fluxed surface layers can expose fresh metal surfaces to the aggressive thermochemical environment, thereby sustaining cumulative section loss.

Recent studies on wall-bounded heat transfer and near-wall transport processes further highlight the sensitivity of local wall heat flux and surface exposure to solid–fluid thermal coupling and flow conditions [23,24]. Numerical investigations based on the lattice Boltzmann method have shown that localized wall heat flux can vary significantly depending on near-wall thermal coupling and flow structure [23]. In addition, studies on impurity-mediated slip reduction indicate that surface deposits or impurity particles can substantially alter near-wall momentum transfer and surface interaction processes [24]. These findings provide a broader transport-physics context for interpreting the localized thermal loading and flow-assisted removal mechanisms discussed in the present case study.

The coupled thermochemical corrosion and flow-assisted removal framework is schematically illustrated in Fig. 12(a), which summarizes the concurrent roles of thermal loading, chemical weakening of surface layers, gas-flow interaction, and progressive metal recession. The inset in Fig. 12(b) illustrates the conceptual evolution of surface-layer thickness $x(t)$ and cumulative metal loss $\delta(t)$, which may exhibit non-linear temporal behavior due to the interaction between corrosion growth and intermittent layer removal.

Under flame-facing conditions, the grate-bar surface temperature T_s is governed by the combined effects of radiative heat transfer from the flame and convective heat transfer from the hot flue gas. The net thermal flux imposed on the grate surface may be conceptually expressed as

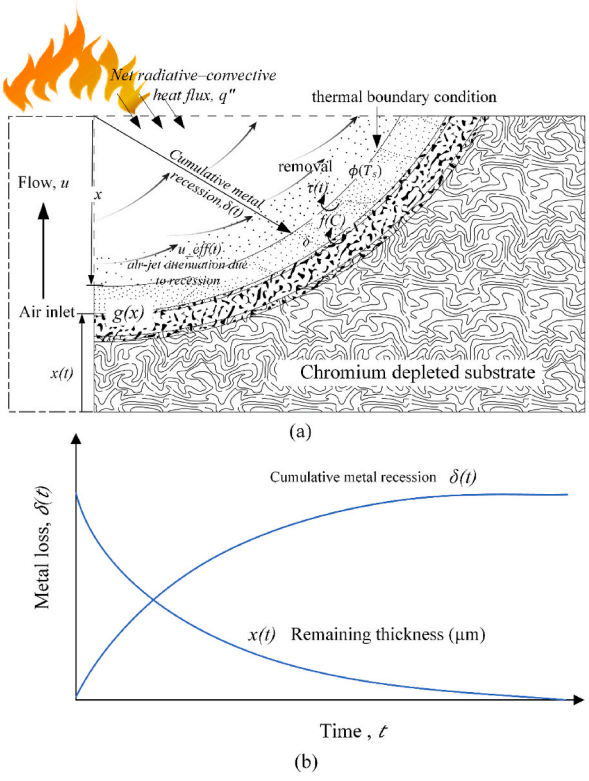

Fig. 12. (a) Conceptual schematic of the coupled thermochemical corrosion and flow-assisted removal framework describing grate degradation under biomass-fired conditions. (b) Conceptual evolution of surface-layer thickness $x(t)$ and cumulative metal loss $\delta(t)$, illustrating non-linear degradation associated with repeated cycles of corrosion-layer growth and removal.

$$q'' = \varepsilon\sigma\left(T_f^4 - T_s^4\right) + h\left(T_g - T_s\right) \tag{1}$$

where ε is the surface emissivity, σ is the Stefan–Boltzmann constant, h is the convective heat-transfer coefficient, T_f is flame temperature, T_g is gas temperature, and T_s is surface temperature. where radiative heat transfer is expected to dominate at leading-edge regions with direct flame exposure. The resulting surface temperature T_s strongly influences corrosion kinetics and the mechanical stability of oxide and fluxed surface layers.

The evolution of the mechanically active surface layer $x(t)$ can be conceptually described as the balance between diffusion-controlled growth and flow-assisted removal. Consistent with classical oxidation behavior and the porous morphologies observed in SEM images, surface-layer growth may follow parabolic-type kinetics and can be expressed as

$$\left(\frac{dx}{dt}\right)_{\text{growth}} = \frac{k_p\, f(C)}{x} \tag{2}$$

where k_p is an effective parabolic growth constant dependent on surface temperature T_s and local ash chemistry $f(C)$, including alkali, chlorine, and silicon species.

In parallel, removal of the mechanically weakened layer may be enhanced by gas-flow interaction and temperature-dependent softening of alkali–silicate deposits. A key feature of the present framework is that the effective flow intensity near the surface may change as metal recession alters the local geometry. Cumulative metal loss $\delta(t)$ can therefore reduce the effectiveness of impinging air jets, leading to a gradual decrease in the effective near-surface velocity $u_{\text{eff}}(t)$ and the associated shear stress $\tau(t)$.

Accordingly, the conceptual evolution of the surface layer may be expressed as

$$\frac{dx}{dt} = \frac{k_p\, f(C)}{x} - k_r\, \tau(t)\, \phi(T_s)\, g(x) \tag{3}$$

where k_r is an effective removal coefficient, $\phi(T_s)$ represents temperature-dependent softening or weakening of fluxed deposits, and $g(x)$ accounts for the shielding effect of the surface layer.

The corresponding cumulative metal loss can be expressed as

$$\frac{d\delta}{dt} = k_m\, \tau(t)\, \phi(T_s)\, g(x) \tag{4}$$

where k_m represents an effective metal-loss coefficient. This formulation conceptually yields smooth degradation trajectories and conceptually reproduces the non-linear metal-loss behavior illustrated in Fig. 12(b).

The coupling between Eqs. (3) and (4) leads to alternating phases of relatively slow degradation during surface-layer accumulation and accelerated metal loss following layer thinning or detachment. This behavior is consistent with the irregular and spatially non-uniform section loss observed in the failed grate bars.

Although the coupled behavior shares conceptual similarities with thermomechanical erosion models developed for heterogeneous materials under reacting flows [25], the physical interpretation differs. In biomass-fired grate systems, gas flow does not directly erode the bulk metal; rather, it regulates surface exposure by removing corrosion-weakened oxide and fluxed layers, while the underlying metal recession remains primarily governed by thermochemical corrosion processes.

It is emphasized that Eqs. (1)–(4) constitute a mechanism-based interpretive framework developed to rationalize the observed degradation trends and SEM–EDS observations. The framework is therefore intended to provide a physically consistent explanation of the observed degradation behavior rather than a calibrated life-prediction model and should be interpreted qualitatively in the absence of direct flow-field measurements.

4.6. Limitations of the present study

Although the present study provides insight into the degradation behavior of GX130CrSi29 grate bars under biomass-fired conditions, several limitations should be acknowledged. First, the investigation is based on a limited number of representative grate-bar specimens retrieved from a single industrial biomass furnace. While the observed multilayer corrosion architecture and elemental distributions were consistent across the analyzed samples, the results should be interpreted as representative case-study observations rather than statistically generalized corrosion behavior.

Second, direct crystallographic phase identification of the corrosion products was not performed. The interpretation of degradation mechanisms is therefore based on the combined analysis of microstructural morphology and elemental distributions obtained from SEM/EDS together with comparison to corrosion mechanisms reported in the literature for biomass combustion environments. Although this approach provides strong contextual evidence, additional phase-sensitive techniques such as X-ray diffraction or electron diffraction could provide further confirmation of specific corrosion phases.

Third, the proposed framework linking thermochemical corrosion with flow-assisted removal of corrosion-weakened surface layers is interpretive in nature. Direct measurements of local flow fields, erosion forces, or time-resolved layer detachment were not available in the present industrial case study. Consequently, the framework should be regarded as a conceptual explanation for the observed non-uniform degradation patterns rather than as a calibrated predictive model.

Despite these limitations, the analysis of service-exposed grate bars from a full-scale operating furnace provides valuable practical

insight into biomass-specific degradation mechanisms under real industrial operating conditions.

5. Conclusions

This study applied a practical failure-analysis approach to investigate the degradation behavior of GX130CrSi29 grate bars retrieved from a full-scale biomass-fired furnace. Based on macroscopic inspection, cross-sectional SEM observations, and EDS-derived elemental distributions, the following conclusions can be drawn:

1. The degradation of GX130CrSi29 grate bars appears to be governed primarily by environment-driven thermochemical processes under biomass-fired furnace conditions rather than by localized material defects or alloy variability. Despite position-dependent differences in damage severity, all investigated samples exhibit a consistent multilayer corrosion architecture, suggesting a common degradation pathway controlled by furnace thermochemical and operating conditions.
2. Although GX130CrSi29 is a high-chromium cast alloy, only a thin and locally discontinuous chromium-enriched inner oxide was observed. SEM/EDS observations indicate significant chromium depletion near the oxide–metal interface, suggesting that chromium-based protective oxides are progressively destabilized under biomass-fired operating conditions.
3. The presence of alkali-bearing ash species (K, Ca, and Si) together with chlorine-containing deposits is consistent with degradation processes involving chlorine-assisted active oxidation and alkali–silicate-related fluxing. These interacting processes appear to promote chromium depletion, porous iron-rich oxide formation, and repeated oxide disruption rather than uniform high-temperature oxidation alone.
4. Oxygen ingress into the chromium-depleted substrate is associated with internal oxidation and localized grain-boundary attack beneath the corrosion scale. These subsurface degradation features are consistent with progressive weakening of the alloy once the protective oxide barrier becomes unstable.
5. The overall degradation behavior can be interpreted using a coupled framework in which thermochemical corrosion weakens oxide and deposit layers while furnace gas flow may facilitate their removal. Repeated exposure of fresh metal surfaces under such conditions can contribute to accelerated and spatially non-uniform section loss. These findings suggest that the use of high-chromium cast alloys alone may not be sufficient to ensure long-term grate durability in alkali–chloride-rich biomass combustion environments.

From an engineering perspective, these findings highlight that effective mitigation may therefore require an integrated approach combining appropriate material selection, management of alkali- and chlorine-rich deposits, and grate design or operational practices that reduce local thermal and chemical exposure, particularly at flame-facing leading-edge regions.

CRediT authorship contribution statement

Wirasak Khongkaew: Writing – review & editing, Writing – original draft, Visualization, Methodology, Investigation, Formal analysis, Conceptualization. **Natt Makul:** Resources, Investigation, Data curation. **Kewalee Nilgumhang:** Investigation, Data curation. **Phadungsak Rattanadecho:** Writing – review & editing, Supervision, Resources.

Declaration of competing interest

The authors declare the following financial interests/personal relationships which may be considered as potential competing interests: Phadungsak Rattanadecho reports that administrative support, equipment, and research resources were provided by the Thailand Science Research and Innovation Fundamental Fund for the fiscal year 2024. Wirasak Khongkaew reports that equipment, research resources, and data analysis support were provided by Thai Solar Energy Public Company Limited (experimental case study context).

If there are other co-authors not listed above, they declare that they have no known competing financial interests or personal relationships that could have appeared to influence the work reported in this paper.

Acknowledgments

The authors gratefully acknowledge the Thailand Science Research and Innovation Fundamental Fund for fiscal years 2024–2025, and Thai Solar Energy Public Company Limited, the power plant owner in this case study, for their support and collaboration.

Data availability

Data will be made available on request.

References

[1] A. Williams, J.M. Jones, L. Ma, M. Pourkashanian, Pollutants from the combustion of solid biomass fuels, Prog. Energy Combust. Sci. 38 (2012) 113–137, https://doi.org/10.1016/j.pecs.2011.07.001.

[2] S.K. Kær, Straw combustion on slow-moving grates—A comparison of model predictions with experimental data, Biomass Bioenergy 28 (2005) 307–320, https://doi.org/10.1016/j.biombioe.2004.08.017.
[3] C. Yin, L. Rosendahl, S.K. Kær, Characterizing and modeling of an 88 MW grate-fired boiler burning wheat straw, Energy 41 (2012) 473–482, https://doi.org/10.1016/j.energy.2012.02.050.
[4] N.T.M. Duffy, J.A. Eaton, Investigation of 3D flow and heat transfer in solid-fuel grate combustion: measures to reduce high-temperature degradation, Combust. Flame 168 (2016) 1–22, https://doi.org/10.1016/j.combustflame.2015.12.032.
[5] R.P. Van der Lans, L.T. Pedersen, A. Jensen, P. Glarborg, K. Dam-Johansen, Modelling and experiments of straw combustion in a grate furnace, Biomass Bioenergy 19 (2000) 199–208, https://doi.org/10.1016/S0961-9534(00)00033-7.
[6] N. Razmjoo, H. Sefidari, M. Strand, Measurements of temperature and gas composition within the burning bed of wet woody residues in a 4 MW moving-grate boiler, Fuel Process. Technol. 152 (2016) 438–445, https://doi.org/10.1016/j.fuproc.2016.07.011.
[7] N. Razmjoo, H. Sefidari, M. Strand, Characterization of hot gas in a 4 MW reciprocating-grate boiler, Fuel Process. Technol. 124 (2014) 21–27, https://doi.org/10.1016/j.fuproc.2014.02.011.
[8] H. Sefidari, N. Razmjoo, M. Strand, Combustion and emissions of two types of woody biomass in a 12 MW reciprocating-grate boiler, Fuel 135 (2014) 120–129, https://doi.org/10.1016/j.fuel.2014.06.051.
[9] H.-H. Frey, B. Peters, V. Scherer, Characterization of municipal solid waste combustion in a grate furnace, Waste Manag. 23 (2003) 689–701, https://doi.org/10.1016/S0956-053X(02)00070-3.
[10] H. Thunman, B. Leckner, Ignition and propagation of a reaction front in cross-current bed combustion of wet biofuels, Fuel 80 (2001) 473–481, https://doi.org/10.1016/S0016-2361(00)00127-7.
[11] H. Thunman, B. Leckner, F. Niklasson, Composition of volatile gases and thermochemical properties of wood for modeling of fixed or fluidized beds, Energy Fuel. 15 (2001) 1488–1497, https://doi.org/10.1021/ef010097q.
[12] M.R. Karim, J. Naser, CFD modelling of combustion and associated emission of wet woody biomass in a 4 MW moving-grate boiler, Fuel 222 (2018) 656–674, https://doi.org/10.1016/j.fuel.2018.02.195.
[13] X. Fan, X. Wang, Z. Ji, X. Li, M. Gan, Y. Wang, H. Zheng, X. Chen, Z. Sun, X. Huang, Physico-chemical profile and corrosion mechanism of the failure grate bar from iron ore sintering process, J. Mater. Res. Technol. 20 (2022) 428–439, https://doi.org/10.1016/j.jmrt.2022.07.130.
[14] H. Asteman, M. Spiegel, Investigation of HCl(g) attack on pre-oxidized pure Fe, Cr, Ni and commercial 304 steel at 400 °C, Corros. Sci. 49 (2007) 3626–3637, https://doi.org/10.1016/j.corsci.2007.03.028.
[15] M. Hänsel, C.A. Boddington, D.J. Young, Internal oxidation and carburisation of heat-resistant alloys, Corros. Sci. 45 (2003) 967–981, https://doi.org/10.1016/S0010-938X(02)00182-8.
[16] I.M. Allam, Z.M. Gasem, High temperature corrosion of alloy haynes 556 in carburizing/oxidizing environments, Mater. Corros. 58 (2005) 245–253, https://doi.org/10.1002/maco.200604011.
[17] X. Li, Y. Wang, T. Allgurén, K. Andersson, J.O.L. Wendt, The roles of added chlorine and sulfur on ash deposition mechanisms during solid fuel combustion, Proc. Combust. Inst. 38 (3) (2021) 4309–4316, https://doi.org/10.1016/j.proci.2020.10.003.
[18] M. Spiegel, H.J. Grabke, A. Zahs, Influence of chlorine and alkali chlorides on high-temperature corrosion of steels, Corros. Sci. 47 (12) (2005) 2931–2951.
[19] M. Spiegel, Chlorine-induced corrosion in power plant materials, in: Materials Degradation and Corrosion Control in Power Systems, Woodhead Publishing, Cambridge, 2010, pp. 67–98.
[20] C. Berlanga-Labari, J. Fernández-Carrasquilla, High-temperature corrosion of superheater steels in biomass and waste-fired boilers, Mater. Corros. 57 (7) (2006) 543–551.
[21] J. Lehmusto, T. Varis, M. Hupa, Corrosion of steel materials by molten alkali silicates in biomass combustion environments, Fuel 90 (5) (2011) 2017–2024, https://doi.org/10.1016/j.fuel.2011.01.021.
[22] Y. Liu, W. Fan, X. Wu, X. Zhang, Chlorine-induced high-temperature corrosion of boiler steels combusting sha erhu coal compared to biomass, Energy Fuel. 32 (4) (2018) 4237–4247, https://doi.org/10.1021/acs.energyfuels.7b03143.
[23] Y. Sun, C. Shao, et al., A between-wall heat transfer simulation approach based on the lattice boltzmann method and its application in tube heat transfer analysis, Case Stud. Therm. Eng. 58 (2024) 104437, https://doi.org/10.1016/j.csite.2024.104437.
[24] Y. Sun, D. Bian, Y. Wang, Z. Li, Effects of impurity particles on flow slip on grooved surfaces, Phys. Rev. Fluids 10 (9) (2025) 094202, https://doi.org/10.1103/h6s7-2z44.
[25] Y.I. Dimitrienko, I.D. Dimitrienko, Effect of thermomechanical erosion on heterogeneous combustion of composite materials in high-speed flows, Combust. Flame 122 (2000) 211–222, https://doi.org/10.1016/S0010-2180(00)00124-3.
[26] S. Hermansson, H. Thunman, Measures to reduce grate material wear in fixed-bed combustion, Energy Fuel. 25 (2011) 1387–1395, https://doi.org/10.1021/ef101473b.